Journal of Advanced Ceramics
2022, **11**(4): 545–555
https://doi.org/10.1007/s40145-021-0554-2
ISSN 2226-4108
CN 10-1154/TQ

Research Article

Achieving ultra-broadband electromagnetic wave absorption in high-entropy transition metal carbides (HE TMCs)

Weiming ZHANG[a], Huimin XIANG[a], Fu-Zhi DAI[a], Biao ZHAO[b], Shijiang WU[c], Yanchun ZHOU[a,*]

[a]*Science and Technology on Advanced Functional Composite Laboratory, Aerospace Research Institute of Materials & Processing Technology, Beijing 100076, China*
[b]*Henan Key Laboratory of Aeronautical Materials and Application Technology, School of Material Science and Engineering, Zhengzhou University of Aeronautics, Zhengzhou 450046, China*
[c]*Zibo Firststar New Material Incorporated Co., Ltd., Zibo 255000, China*

Received: August 11, 2021; Revised: November 1, 2021; Accepted: November 9, 2021

Abstract: Electronic devices pervade everyday life, which has triggered severe electromagnetic (EM) wave pollution. To face this challenge, developing EM wave absorbers with ultra-broadband absorption capacity is critically required. Currently, nano-composite construction has been widely utilized to realize impedance match and broadband absorption. However, complex experimental procedures, limited thermal stability, and interior oxidation resistance are still unneglectable issues. Therefore, it is appealing to realize ultra-broadband EM wave absorption in single-phase materials with good stability. Aiming at this target, two high-entropy transition metal carbides (HE TMCs) including (Zr,Hf,Nb,Ta)C (HE TMC-2) and (Cr,Zr,Hf,Nb,Ta)C (HE TMC-3) are designed and synthesized, of which the microwave absorption performance is investigated in comparison with previously reported (Ti,Zr,Hf,Nb,Ta)C (HE TMC-1). Due to the synergistic effects of dielectric and magnetic losses, HE TMC-2 and HE TMC-3 exhibit better impedance match and wider effective absorption bandwidth (EAB). In specific, the exclusion of Ti element in HE TMC-2 endows it optimal minimum reflection loss (RL_{min}) and EAB of −41.7 dB (2.11 mm, 10.52 GHz) and 3.5 GHz (at 3.0 mm), respectively. Remarkably, the incorporation of Cr element in HE TMC-3 significantly improves the impedance match, thus realizing EAB of 10.5, 9.2, and 13.9 GHz at 2, 3, and 4 mm, respectively. The significance of this study lays on realizing ultra-broadband capacity in HE TMC-3 (Cr, Zr, Hf, Nb, Ta), demonstrating the effectiveness of high-entropy component design in tailoring the impedance match.

Keywords: transition metal carbide (TMC); high-entropy ceramics; electromagnetic (EM) wave absorption; dielectric and magnetic loss coupling; ultra-broadband absorption

1 Introduction

The ever-growing demands for communication capacity have spurred advancing in microwave engineering, which in turn results in massive electromagnetic (EM) wave pollution that could pose a threat to human health [1–3]. To eliminate this adverse effect, EM wave absorbers with ultra-broadband effective absorption capability are the targets of many current researches,

* Corresponding author.
E-mail: yczhou@alum.imr.ac.cn

which possess superior applicability across wide frequency bands [3–6]. Thus, there have been intense research efforts in exploiting effectual strategy for designing ultra-broadband EM wave absorbers [7–9].

A perusal of the literature reveals that nano-composite construction has been taken for granted as the most effective way in realizing broadband absorption. By combining dielectric loss-type nanomaterials (C [10–12], intrinsic conducting polymer [13], MXenes [14], SiC [15,16], etc.) with magnetic loss-type nanomaterials (Fe_3O_4 [17], Fe_3S_4 [18], CoS_2 [19], etc.), it is effective to realize ideal impedance match and broadband absorbing capacity, which are ascribed to the enhanced interfacial polarization loss capability and the coupling effects of dielectric and magnetic losses [5]. However, the complex experimental procedures and the difficulty in precisely controlling the nanostructure and dispersibility of nanofillers are the main drawbacks of this paradigm. Besides, the magnetic loss capability derived from magnetic nanofillers may come across a sudden reduction over the Curie or Neel temperature [3]. Moreover, unsatisfied thermal stability and oxidation resistance are also unneglectable issues for high-temperature applications [20]. Therefore, it is appealing to explore EM absorbers with good thermal stability and high-efficient absorption performance which can be synthesized by an easy fabrication method.

By virtue of the co-existence of covalent bonding, ionic bonding, and metallic bonding, transition metal monocarbides (TMCs) are characterized by high melting point, high hardness, and good chemical stability together with high thermal and electrical conductivities, which have been utilized as cutting and grinding tools for abrasive industry, high-temperature materials for aerospace industry, and conductive devices for microelectronics industry [21–25]. Very recently, TMCs have been found highly efficient as EM wave absorbers, in which the dielectric loss capacity is originated from the metallic feature of TMCs, and the magnetic loss capacity is derived from TM-d orbital splitting [26]. As demonstrated by Zhou *el al*. [26], HfC and TaC possess strong and broadband absorption capability due to the synergistic effects of dielectric and magnetic losses. Combining excellent thermal stability and EM wave absorption performance, single-phase TMCs prepared by a simple one-pot carbothermal reduction method are promising as candidates for high-temperature EM wave absorbers. However, their applications are hindered by heavy weight, which requires further modifications.

High-entropy construction is a useful design strategy for weight reduction; however, high-entropy (Ti,Zr,Hf, Nb,Ta)C with lower density exhibits poorer EM wave absorption performance compared with those of HfC and TaC, which is ascribed to the presence of TiC with intense discrepancy between the dielectric and magnetic losses [26]. In our previous studies [27–30], high-entropy compositional design has been found effectively in improving impedance match and EM wave absorption performance. Notably, the incorporation of Cr in high-entropy transition metal diboride (HE TMB_2) leads to strong and broadband absorption capacity [30]. Therefore, through eliminating Ti element or substituting Ti element with Cr element, it is expected that the EM wave absorption performance of HE TMCs can be further improved.

Aiming at achieving better EM wave absorption performance than that of high-entropy (Ti,Zr,Hf,Nb,Ta)C (HE TMC-1), two nominally equimolar HE TMCs including (Zr,Hf,Nb,Ta)C (HE TMC-2) and (Cr,Zr,Hf, Nb,Ta)C (HE TMC-3) are designed as new EM wave absorbers. Note that the data of HE TMC-1 (TM = Ti, Zr, Hf, Nb, Ta) in this study are cited from Ref. [26]. Through high-entropy engineering, it is expected that the formation of HE TMCs would be beneficial to enhance the overall properties including thermal stability [31–33], oxidation, and corrosion resistance [34,35], as well as EM wave absorption performance [36].

2 Materials and method

2. 1 Synthesis of HE TMC powders

To address the purpose of improving EM absorption performance, two nominally equimolar HE TMCs, i.e., (Zr,Hf,Nb,Ta)C and (Cr,Zr,Hf,Nb,Ta)C, were designed and subsequently synthesized by carbothermal reduction method according to Reactions (1) and (2):

$$2ZrO_2 + 2HfO_2 + Nb_2O_5 + Ta_2O_5 + 26C = 8(Zr_{0.25}Hf_{0.25}Nb_{0.25}Ta_{0.25})C + 18CO \quad (1)$$

$$Cr_2O_3 + 2ZrO_2 + 2HfO_2 + Nb_2O_5 + Ta_2O_5 + 31C = 10(Zr_{0.25}Hf_{0.25}Nb_{0.25}Ta_{0.25})C + 21CO \quad (2)$$

The starting reactants including transition metal oxides (Cr_2O_3, ZrO_2, HfO_2, Nb_2O_5, and Ta_2O_5, 99.9% purity, 1 μm; China New Materials Technology Co., Ltd., Beijing, China) and carbon black (99% purity, −100 mesh; Mudanjiang Qianjin Reagent Co., Ltd.,

Heilongjiang, China) were weighted according to Reactions (1) and (2), and then mixed thoroughly in an agate mortar. The mixed powders were uniaxially pelletized into cylindrical pellets using a stainless-steel die with the diameter of 12 mm, which were heated at 1950 ℃ for 1 h in vacuum. Finally, the as-prepared pellets were crushed, ground in an agate mortar, and then sieved through a 120-mesh screen for subsequent characterizations.

2. 2 Characterizations

Phase composition was analyzed by an X-ray diffractometer (XRD; D8 Advanced, Bruker, Germany) utilizing Cu Kα radiation (λ = 1.5418 Å) with a step size of 0.02° at a scanning rate of 2 (°)/min. The lattice parameter was obtained by Rietveld refinement using the total pattern solution software (TOPAS; Bruker Corp., Karlsruhe, Germany). A SUPRA 35 scanning electron microscope (SEM; LEO, Oberkochen, Germany) equipped with the energy disperse spectroscopy (EDS) was used for morphology observation. The chemical compositions were analyzed using an inductively-coupled plasma atomic emission spectrometer (ICP-AES; Thermo iCAP 6000 series, Thermo Fisher Scientific Inc., Waltham, MA, USA) using the samples prepared by the following procedures. The as-prepared powders were mixed with sodium peroxide and sodium hydroxide, and then decomposed at 700 ℃ for 15 min. The obtained melts were acidified with hydrochloric acid, which were finally aspirated into the device.

The relative complex permittivity ($\varepsilon_r = \varepsilon' + j\varepsilon''$) and permeability ($\mu_r = \mu' + j\mu''$) were determined by a vector network analyzer (Agilent N5244A, USA) using the coaxial method in the frequency range of 1.0−18.0 GHz. The as-prepared HE TMC powders and paraffin wax were mixed at a mass ratio of 7:3 and compacted into a toroidal shape (Φ_{out} = 7.00 mm, Φ_{in} = 3.04 mm). Based on the transmission-line theory and metal back-panel model, the reflection loss (RL) was determined from the relative complex permittivity and permeability for a given frequency and sample thickness according to Eqs. (3) and (4) [6,7]:

$$\mathrm{RL(dB)} = 20\log\left|(Z_{in} - Z_0)/(Z_{in} + Z_0)\right| \quad (3)$$

$$Z_{in} = Z_0\sqrt{\frac{\mu_r}{\varepsilon_r}}\tanh\left(j\frac{2\pi fd\sqrt{\mu_r\varepsilon_r}}{c}\right) \quad (4)$$

where Z_0 represents the impedance of free space, Z_{in} represents the normalized input characteristic impedance at the interface between atmosphere and absorber, μ_r is the relative complex permeability, ε_r is the relative complex permittivity, f is the frequency, d is the thickness of samples, and c is the velocity of light (3×10^8 m/s). The effective absorption bandwidth (EAB) is defined by the frequency range over which the RL value is smaller than −10 dB, which is comparable to 90% microwave energy absorption [6,7].

3 Results and discussion

As shown in Fig. 1(a), TMCs crystalize in B1 (NaCl) structure with the space group of $Fm\bar{3}m$ (No. 225) consisting of TMC_6 octahedral [22]. From Fig. 1(b), it can be interpreted that the TM atoms fill in the octahedral coordination constructed by carbon atoms, which will lead to the elimination of degeneracy of TM-d orbitals due to the crystal field effects [37–39]. In specific, the electrons in e_g (d_{z^2} and $d_{x^2-y^2}$) orbitals suffer a greater repulsion, which is ascribed to that the overlap of e_g orbitals and C-2p orbitals endows e_g orbitals with higher energy levels [38,39]. As for t_{2g} orbitals, they are granted with lower energy levels. Notably, the interconversion between e_g and t_{2g} orbitals as responses to EM field or heat will yield substantial magnetic loss capacity [26].

3. 1 Synthesis and characterization of HE TMCs

With the presence of strong chemical bonding, TMCs

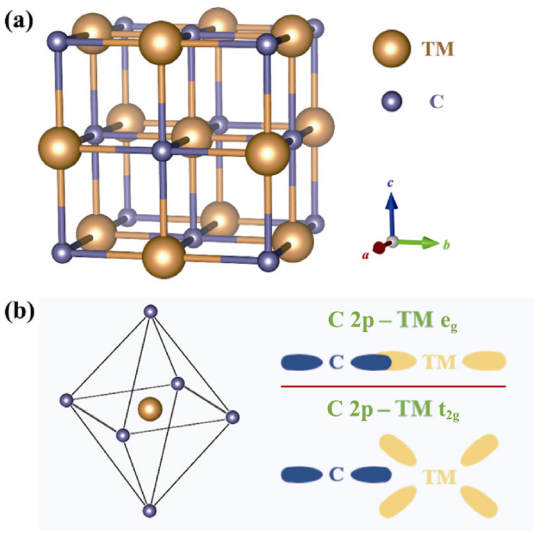

Fig. 1 (a) Crystal structure of TMCs, (b) schematic of the octahedral coordination and the interactions between C-2p and TM-d (TM-e_g and TM-t_{2g}) orbitals.

are featured with low diffusion coefficients, making it difficult to prepare single-phase HE TMCs [23]. As shown in Fig. 2, the formation of HE TMC-1 (TM = Ti, Zr, Hf, Nb, Ta) solid solution after synthesized at 1900 ℃ with the dwelling time of 2 h is incomplete. It is proposed that the trap of TiC with the fastest diffusion rate among TMCs (TM = Ti, Zr, Hf, Nb, Ta) into TaC "host" leads to the shrinkage of the lattice, making it harder for the other TMs to diffuse into the preformed solid solution [40]. As for HE TMC-2 (TM = Zr, Hf, Nb, Ta) synthesized at 1950 ℃ for 1 h, however, the phase separation still exists after the exclusion of Ti element, which is consistent with the previously reported results at even higher calcining temperatures [41]. Notably, the introduction of Cr into HE TMC-3 (TM = Cr, Zr, Hf, Nb, Ta) is helpful to boosting the formation of solid solution, which could be ascribed to the spurred mass transformation induced by the evaporation of Cr_2O_3 at high temperature in vacuum [30]. From Fig. 3, XRD patterns of ZrC, HfC, NbC, and TaC are presented to prove the formation of NaCl-type HE TMC-3 phase. It is worth noting that though there is no experimental evidence of the existence of CrC, the main reflection peaks are indexed as NaCl-type phase, indicating that the as-prepared HE TMC-3 is structurally ordered but compositionally disordered with multi-TM elements (TM = Cr, Zr, Hf, Nb, Ta). Besides, minor impurities detected in the vicinity of (111) plane are indexed as HfC phase, which ranks latest in the sequence of multi-step solid solution formation [42]. Noting that the presence of minor impurities has undamaging and trivial effects on the EM absorption performance, i.e., the impurities could spur the interfacial polarizations, which is trivial when compared with the effect of elemental alternation [26,27]. To determine the final elemental composition of as-prepared HE TMC-2 and HE TMC-3, ICP-AES experiments were conducted. Table 1 lists the nominal and experimental measured compositions. The elemental ratios of TM cations in HE TMC-2 exhibit nearly equimolar, while Cr-deficient scenario is found in HE TMC-3. On the one hand, the severe evaporation of Cr_2O_3 at elevated temperature in vacuum may spur the formation of single-phase HE TMC-3. On the other hand, however, it leads to the limited solid solution quantity of CrC. Through Rietveld refinement, the lattice parameter (a) of HE TMC-3 is determined to be 4.5488 Å, and the theoretical density (ρ) of HE TMC-3 based on ICP-AES results is calculated to be 10.41 g/cm^3, which is effectual in

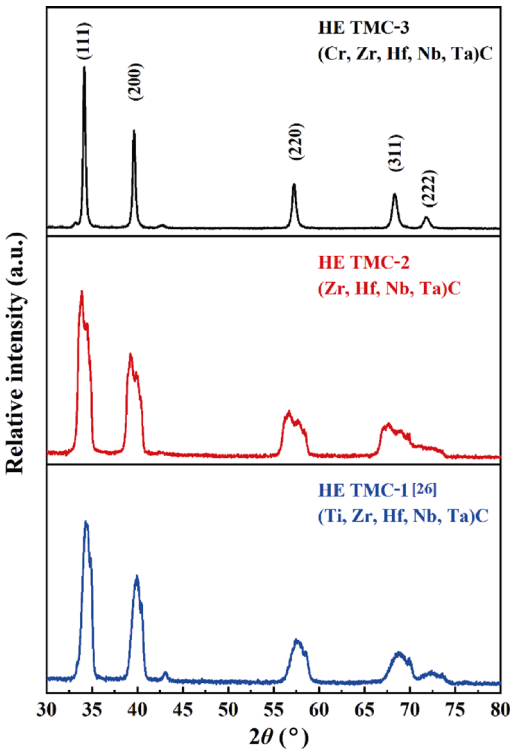

Fig. 2 XRD patterns of HE TMC-1 (TM = Ti, Zr, Hf, Nb, Ta) [26], HE TMC-2 (TM = Zr, Hf, Nb, Ta), and HE TMC-3 (TM = Cr, Zr, Hf, Nb, Ta) powders.

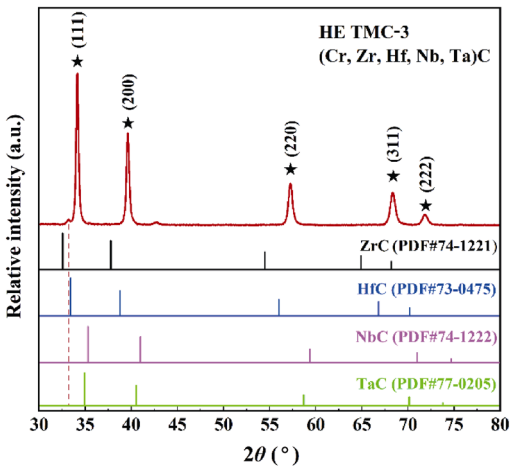

Fig. 3 XRD patterns of HE TMC-3 (TM = Cr, Zr, Hf, Nb, Ta) powders together with those of ZrC, HfC, NbC, and TaC obtained from ICDD/JCPDS cards.

Table 1 Nominal and experimental measured elemental compositions of transition metals (TMs) in as-synthesized HE TMC-2 (TM = Zr, Hf, Nb, Ta) and HE TMC-3 (TM = Cr, Zr, Hf, Nb, Ta)

Composition code	Nominal composition	Measured composition
HE TMC-2	$(Zr_{0.25}Hf_{0.25}Nb_{0.25}Ta_{0.25})C$	$(Zr_{0.245}Hf_{0.250}Nb_{0.255}Ta_{0.250})C$
HE TMC-3	$(Cr_{0.2}Zr_{0.2}Hf_{0.2}Nb_{0.2}Ta_{0.2})C$	$(Cr_{0.004}Zr_{0.241}Hf_{0.244}Nb_{0.258}Ta_{0.253})C$

lowering the density compared with HfC (12.6 g/cm^3) and TaC (14.6 g/cm^3).

Figure 4 illustrates the morphologies of HE TMC-2 (TM = Zr, Hf, Nb, Ta) and HE TMC-3 (TM = Cr, Zr, Hf, Nb, Ta) powders. With the addition of Cr element, HE TMC-3 powders exhibit particle size larger than that of HE TMC-2 powders, which coincides with the situation in high-entropy diboride (HE TMB_2) [30]. The significant growth of HE TMC-3 particles is mainly attributed to the boosted mass transportation due to the evaporation of Cr_2O_3, which is expected to decrease the degree of interfacial polarization and further weaken the dielectric loss capability.

3. 2 EM properties of HE TMC powders

In the light of Maxwell's equations, the interactions between materials and oscillatory EM field can be evaluated by complex permittivity ($\varepsilon_r = \varepsilon' + j\varepsilon''$) and complex permeability ($\mu_r = \mu' + j\mu''$), of which the real parts (ε' and μ') and imaginary parts (ε'' and μ'') represent the energy storage and dissipation capacities, respectively [5].

To reveal the effects of high-entropy compositional design on the EM properties of HE TMCs, Fig. 5 compares the EM parameters of three HE TMCs, where the composition dependent responses to the alternating electric field are observed, i.e., the ε' and ε'' values across the testing frequency range rank roughly in the sequence of HE TMC-1, HE TMC-2, and HE TMC-3. From Figs. 5(b) and 5(c), it is observed that the dielectric loss tangent ($\tan\delta_\varepsilon = \varepsilon''/\varepsilon'$) values exhibit similar frequency dependence as the ε'' values, suggesting that the weakening of dielectric loss capabilities have been achieved by eliminating Ti element in HE TMC-2 and substituting Ti element with Cr element in HE TMC-3. Considering the conductive nature of TMCs, the dielectric loss ability of HE TMCs originates from the conduction loss, the dipolar polarization relaxation loss, and the interfacial polarization relaxation loss (called the Maxwell–Wagner effect) [5,43–45]. In specific, the electron migration contributes to the energy dissipation in the form of conduction loss. Moreover, numerous point defects (e.g., vacancy, substitutional atom, and interstitial atom) existing in the HE TMC solid solutions with multi-principal components can serve as the polarization center, while the local stress induced by lattice disorder can restrain dipole re-orientation under the alternating electric field, thus leading to polarization relaxation with energy consumption [43,44]. Besides, in the heterogeneous HE TMC materials, minor residue impurities and paraffin wax can spur the interfacial polarizations and related relaxations [44]. The polarization relaxation loss process can be determined by Cole–Cole semicircles in Fig. 6(a), of which HE TMC-2 exhibits skewed tendency due to the unignorable conductivity and multi-relaxation processes [5].

From Figs. 5(d) and 5(e), the μ' and μ'' values show explicit distinctions among three HE TMCs, of which the variations are roughly contrary to ε' and ε'' values. As typical dielectric loss-type absorbers, HE TMC-1 exhibits ε' values equal to 1 and negative μ'' values over 4−18 GHz, suggesting that magnetic loss would not operate at these frequency bands [26]. However, the elimination of Ti element in HE TMC-2 leads to the absence of negative μ'' values, which enables EM wave entering the EM wave absorber. Therefore, it can be concluded that the presence of TiC in HE TMC-1 increases the dielectric loss capacity but decreases the magnetic loss capacity, which has detrimental effects on tuning the impedance match. Especially, HE TMC-3 possesses spurred magnetization and magnetic loss

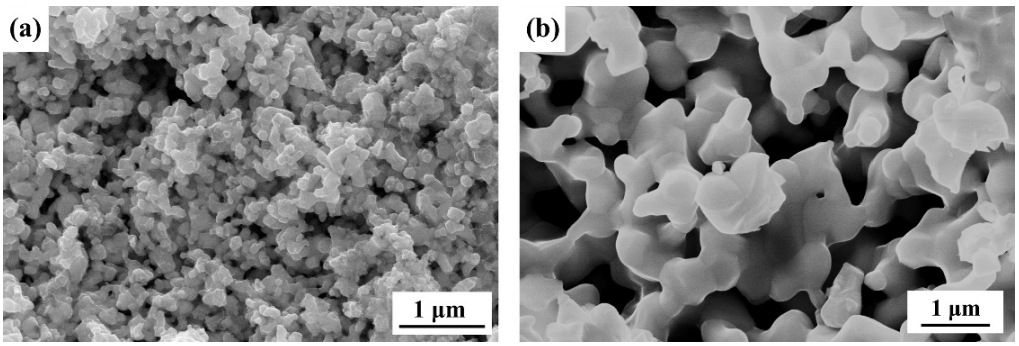

Fig. 4 SEM images of (a) HE TMC-2 (TM = Zr, Hf, Nb, Ta) and (b) HE TMC-3 (TM = Cr, Zr, Hf, Nb, Ta) powders synthesized at 1950 ℃ for the dwelling time of 1 h.

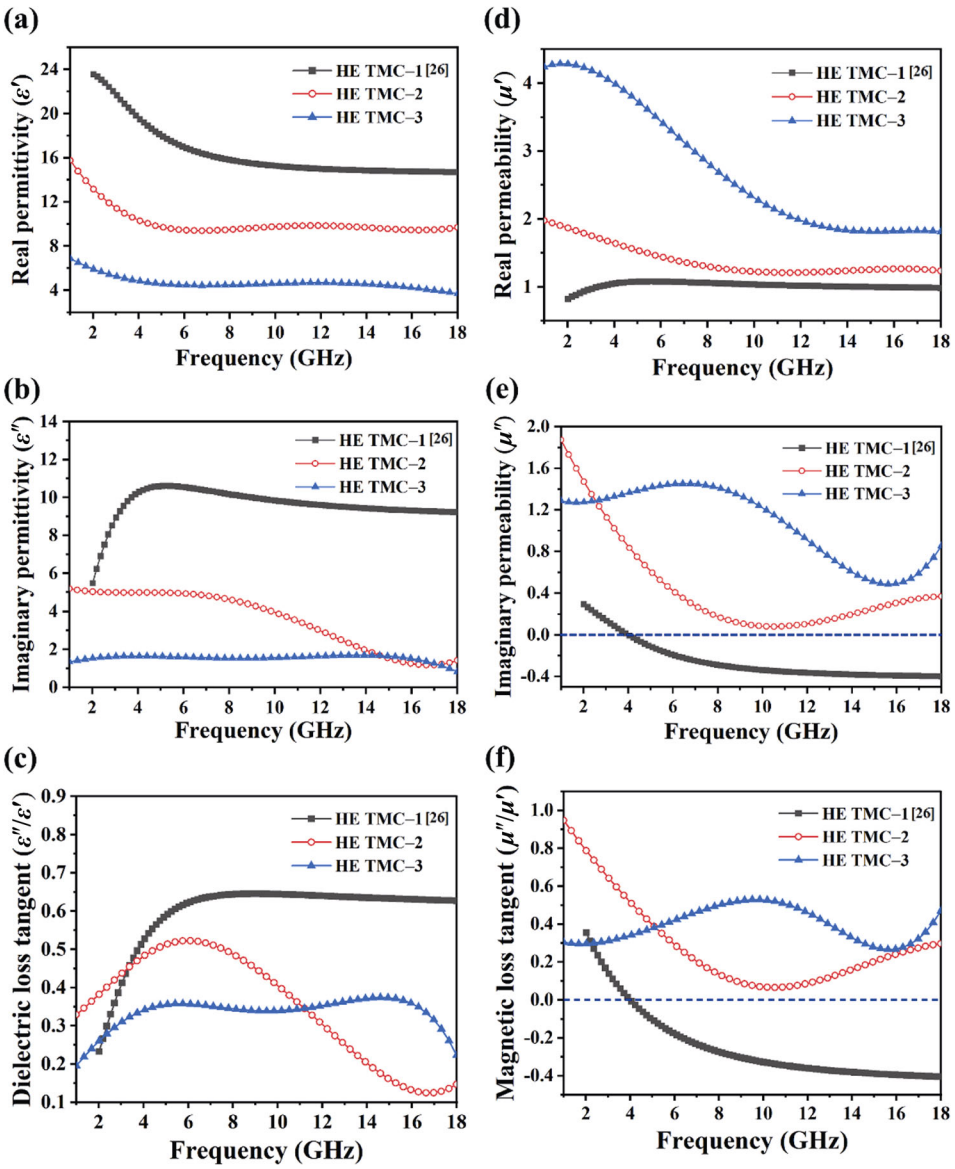

Fig. 5 EM parameters of three HE TMCs: (a) real permittivity (ε'), (b) imaginary permittivity (ε''), (c) dielectric loss tangent ($\varepsilon''/\varepsilon'$), (d) real permeability (μ'), (e) imaginary permeability (μ''), and (f) magnetic loss tangent (μ''/μ'). Note that the EM parameters of HE TMC-1 are obtained from Ref. [26].

capability compared with HE TMC-1 and HE TMC-2, which are ascribed to the partial spin polarization induced by the solid solution of Cr element [30]. As shown in Fig. 5(f), HE TMC-2 and HE TMC-3 possess positive magnetic loss tangent ($\tan\delta_\mu = \mu''/\mu'$) values over the testing frequency span. The $\tan\delta_\mu$–f curve of HE TMC-2 displays a continuous decrease from 1 to 10 GHz and then an insignificant rise from 10 to 18 GHz. As for HE TMC-3, the magnetic loss capability fluctuates in the range of 0.3−0.6, which is comparable to those of magnetic loss-type EM wave absorbers with optimal component designs, e.g., Fe_3O_4 nano-rings [17], Fe_3S_4/rGO nano-composite [18], CoS_2/rGO nano-composite [19], etc. The mechanisms of magnetic loss in three HE TMCs mainly include the resonance loss and the Eddy current loss [5,46,47]. The Eddy current loss can be determined by Eq. (5), which is directly associated with electrical conductivity (σ) and matching thickness (d) [5]:

$$C_0 = \mu''(\mu')^{-2} f^{-1} = 2\pi\mu_0 d^2\sigma \quad (5)$$

where μ_0 is the vacuum permeability. The dominance of resonance loss can be determined by the variation of C_0 values, otherwise the Eddy current loss gains the upper hand. From Fig. 6(b), the stable magnetic loss capability of HE TMC-3 across the whole testing span

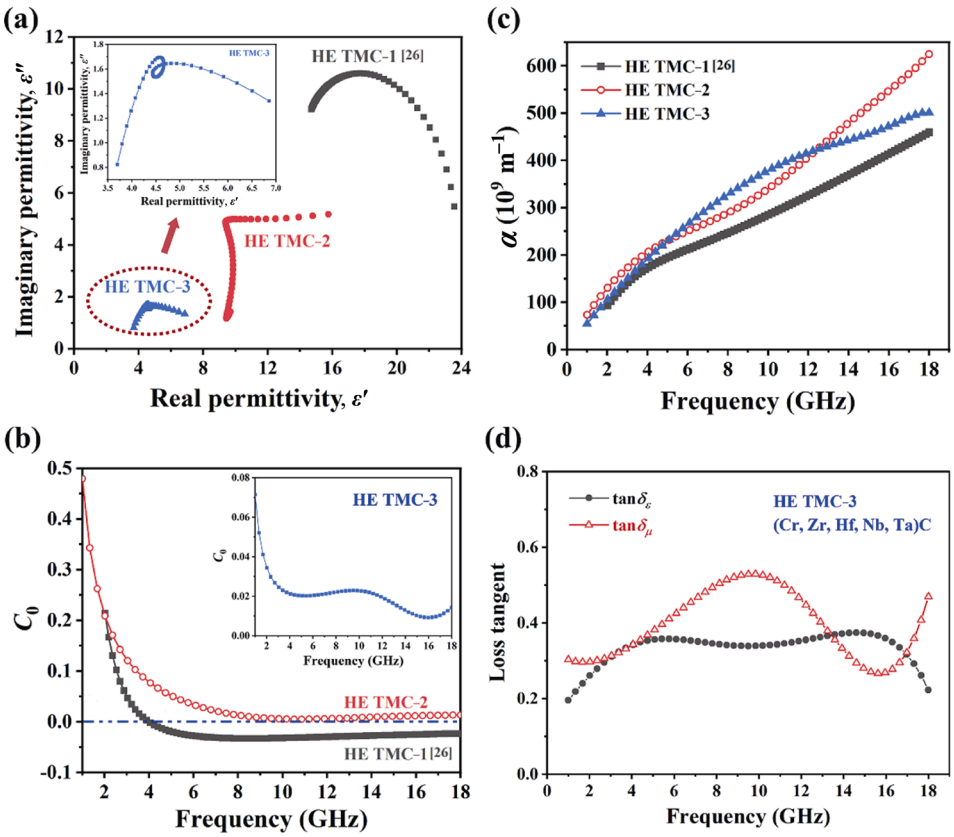

Fig. 6 (a) Cole–Cole semicircles (ε'' vs. ε'), (b) C_0–f curves, (c) attenuation constant α of three HE TMCs, and (d) dielectric and magnetic loss tangents of HE TMC-3.

is attributed to multi-resonance loss, which is related to the d-orbital splitting due to crystal field effect [26,30,37–39] and the electron paramagnetic resonance underpinned by defect energy levels [46,47].

Considering the dielectric and magnetic losses, it is concluded that the synergistic effects of dielectric and magnetic losses are achieved in HE TMC-2 and HE TMC-3, which can be evaluated by the attenuation constant (α), as shown in Fig. 6(c) [7]:

$$\alpha = \frac{\sqrt{2}\pi f}{c} \times \sqrt{(\mu''\varepsilon'' - \mu'\varepsilon') + \sqrt{(\mu''\varepsilon'' - \mu'\varepsilon')^2 + (\mu'\varepsilon'' + \mu''\varepsilon')^2}} \quad (6)$$

Though HE TMC-1 possesses strong dielectric loss, the absence of magnetic loss leads to less satisfactory EM wave dissipation capacity [26]. In addition, the dissipation capacities of HE TMC-2 and HE TMC-3 vary with frequency, i.e., HE TMC-3 possesses larger α values in the frequency range of 5−12 GHz, while HE TMC-2 prevails at the other frequency ranges. Apart from the EM wave dissipation capacity, the impedance matching character plays a critical role in deciding the effective absorption bandwidth [7–9]. As shown in Fig. 6(d), HE TMC-3 exhibits the magnetic loss tangent comparable to the dielectric loss tangent across the testing frequency span, with dielectric loss dominating over 13–17 GHz and magnetic loss dominating over the rest frequency ranges. Considering that the resonance loss capacity of HE TMC-3 is mainly originated from the d-orbital splitting and the electron paramagnetic resonance, HE TMC-3 is expected to maintain high magnetic loss capacity at high temperatures [3,20]. Notably, decreasing the dielectric loss capacity and increasing the magnetic loss capacity in the meantime are helpful in optimizing the impedance match for dielectric loss-type EM wave absorbers with good conductivity, e.g., carbon nanotubes (CNTs) [11], TMCs [26], transition metal diborides (TMB_2s) [48], high-entropy alloys [49,50], etc. Therefore, it is promising to achieve good impedance match in HE TMC-3 with relatively close dielectric and magnetic loss capacities across a wide frequency band.

On the basis of the above analysis, there are two pivotal factors deciding the EM wave absorption performance of HE TMCs, namely, the dissipation

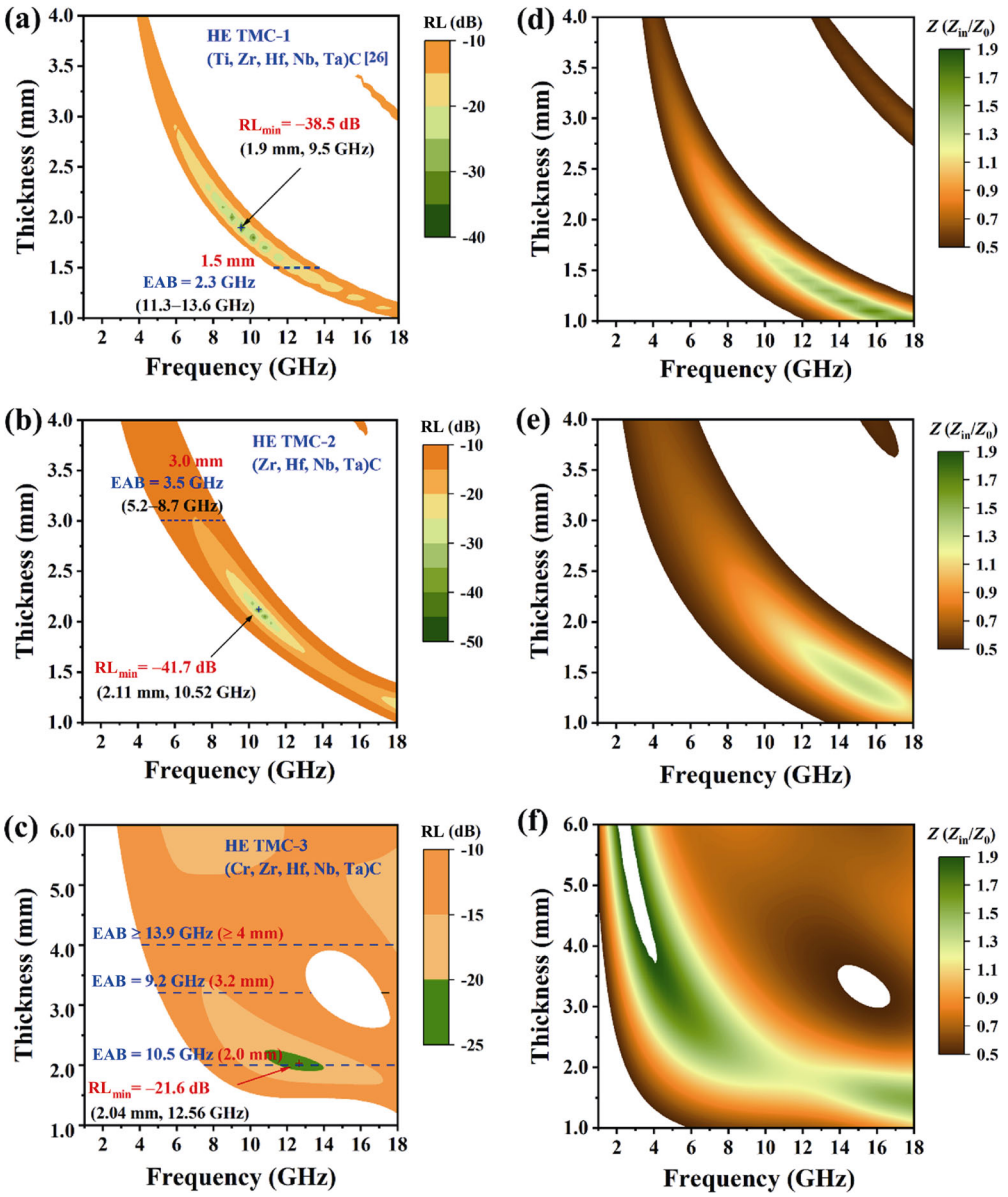

Fig. 7 Contour maps of reflection loss (RL) and impedance match (Z) values of (a, d) HE TMC-1, (b, e) HE TMC-2, and (c, f) HE TMC-3.

capacity (α) and the impedance match (Z), in which the latter directly determines the EAB. To elaborate the effects of impedance match on the effective absorption bandwidth, it can be concluded that the effective absorption takes place when $0.52 \leqslant Z \leqslant 1.93$ by solving Eq. (7) [30,51]:

$$\mathrm{RL(dB)} = 20\log\left|\left(Z_{\mathrm{in}} - Z_0\right)/\left(Z_{\mathrm{in}} + Z_0\right)\right| \leqslant -10\ \mathrm{dB} \quad (7)$$

As shown in Fig. 7, the effective absorption can be achieved in three HE TMCs within the regions where $0.52 \leqslant Z \leqslant 1.93$. From Figs. 7(a)–7(c), the optimal $\mathrm{RL_{min}}$ values at matching frequency and thickness of HE TMC-1, HE TMC-2, and HE TMC-3 are −38.5 dB (1.9 mm, 9.5 GHz), −41.7 dB (2.11 mm, 10.52 GHz), and −21.6 dB (2.04 mm, 12.56 GHz), respectively, which are realized when the impedance match is ideal ($Z \approx 1$). From Figs. 7(d)–7(f), it can be inferred that removing Ti element has a beneficial effect on promoting the impedance match of HE TMCs, which is especially conspicuous for HE TMC-3 with the addition of Cr element. As shown in Fig. 7(f), the frequency band of HE TMC-3 where Z values lie between 0.52 and 1.93 covers almost the whole testing frequency range in spite of the variation of sample thickness. Apart from the ideal impedance matching zone, there are a few areas where impedance mismatch occurs due

to the occasional predominance of dielectric loss capability, as described in Fig. 6(d). As a consequence of tuning the impedance match, the optimal EAB and the corresponding matching thickness of HE TMC-1 and HE TMC-2 are 2.3 GHz (at 1.5 mm) and 3.5 GHz (at 3.0 mm), respectively. As for HE TMC-3, broadband absorption can be realized at various sample thicknesses, i.e., the EABs at 2.0 and 3.2 mm are 10.5 and 9.2 GHz, respectively, while the EABs at thickness over 4 mm are greater than 13.9 GHz. The EAB at 6.0 mm reaches 15.2 GHz (2.8−18 GHz), almost covering the total S band (2−4 GHz), C band (4−8 GHz), X band (8−12 GHz), and Ku band (12−18 GHz). Needless to say, incorporating Cr element in HE TMC-3 significantly broadens the EAB compared with HE TMC-1, making it capable of realizing ultra-broadband absorption. As mentioned before, it has surprisingly been found that the EAB at 4.0 mm reaches 13.9 GHz, which is superior to most other EM wave absorbing materials [7–9]. In addition, the ultra-broadband absorption capability is insensitive to the sample thickness, rendering it highly tolerant to manufactural error. Drawn from the above analysis, it can be concluded that the elimination of Ti element in HE TMC-2 has positive effects on improving EM wave absorption performance, while substituting Ti element with Cr element significantly boosts the magnetic loss capacity and improves the impedance match across the whole testing frequency band, endowing HE TMC-3 ultra-broadband absorption capacity. Therefore, through high-entropy component design, it is effective to optimize the impedance match of HE TMCs, thus achieving ultra-broadband absorption performance. Besides, high-entropy engineering is effective in lowing the density. Table 2 compares the density (ρ) and EM wave absorption performance at the same sample thickness (2 mm) among single-phase TMCs (TM = Ti, Zr, Hf, Nb, Ta), HE TMC-1, HE TMC-2, and HE TMC-3. Note that the densities of single-phase TMCs (TM = Ti, Zr, Hf, Nb, Ta) are obtained from standard ICDD/JCPDS cards (PDF#79-0298, PDF#74-1221, PDF#73-0475, PDF#74-1222, and PDF#77-0205). It can be seen that the weight reduction and the broadening of effective absorption bandwidth are achieved in HE TMC-3 compared with TaC and HfC. Therefore, incorporating CrC in HE TMC-3 meets the needs of exploring TMCs with light weight and broadband absorption performance.

Table 2 Comparison of densities (ρ) and EM wave absorption performance among single-phase TMCs (TM = Ti, Zr, Hf, Nb, Ta) [26], HE TMC-1 [26], HE TMC-2, and HE TMC-3 at the same sample thickness (2 mm)

Compound	ρ (g/cm^3)	RL_{min} (dB)	EAB (GHz)
TiC	4.90	−4.1	0
ZrC	6.74	−14.6	4.1
HfC	12.60	−15.1	5.5
NbC	8.18	−33.8	3.1
TaC	14.58	−41.8	4.6
HE TMC-1	9.42	−27.5	2.1
HE TMC-2	10.53	−31.0	3.4
HE TMC-3	10.41	−21.4	10.5

4 Conclusions

In conclusion, two HE TMCs with nominally equimolar ratio of TM elements including (Zr,Hf,Nb,Ta)C (HE TMC-2) and (Cr,Zr,Hf,Nb,Ta)C (HE TMC-3) are designed and synthesized, of which the EM wave absorption performances are compared with those of previously reported (Ti,Zr,Hf,Nb,Ta)C (HE TMC-1).

XRD analyses indicate that the as-synthesized HE TMC-2 with the exclusion of Ti element compared with HE TMC-1 still exhibits phase segregation, while the incorporation of Cr element in HE TMC-3 boosts the formation of single-phase solid solution. The theoretical density of HE TMC-3 is determined as 10.41 g/cm^3, which exhibits lower density compared with broadband transition metal carbide absorbers including HfC and TaC. Through SEM analyses, the incorporation of Cr element leads to significant growth of particle size, which can further decrease the dielectric loss capability.

Through high-entropy component design, the coupling effects of dielectric and magnetic losses can be effectively tailored, leading to promoted impedance match. Compared with HE TMC-1, the elimination of Ti element in HE TMC-2 leads to positive magnetic loss tangent over the testing frequency span, which prevents the EM wave from being directly reflected at the surface and contributes to the improved dissipation capacity and EAB. The optimal RL_{min} and EAB of HE TMC-2 are −41.7 dB (2.11 mm, 10.52 GHz) and 3.5 GHz (at 3.0 mm), respectively. Notably, the substitution of Ti element with Cr element in HE TMC-3 contributes to close dielectric and magnetic loss tangents across a wide frequency band, making it

capable of realizing ultra-broadband absorption. As a result of ideal impedance match, HE TMC-3 reaches effective absorption bandwidth greater than 13.9 GHz over 4 mm. Moreover, the ultra-broad EAB is insensitive to the variation of sample thickness. Considering excellent thermal stability, good oxidation and corrosion resistance, and ultra-broadband absorption performance, HE TMC-3 (TM = Cr, Zr, Hf, Nb, Ta) exhibits great application potential as EM wave absorbers, especially under high-temperature or corrosive serving environments.

Acknowledgements

We gratefully acknowledge the financial support from the National Natural Science Foundation of China (Nos. 51972089, 51672064, and U1435206).

References

[1] Golio J. *The RF and Microwave Handbook*. Boca Raton, USA: CRC Press, 2001.

[2] Jamshed MA, Héliot F, Brown TWC. A survey on electromagnetic risk assessment and evaluation mechanism for future wireless communication systems. *IEEE J Electromagn RF Microw Med Biol* 2020, **4**: 24–36.

[3] Mishra RK, Dutta A, Mishra P, *et al*. Recent progress in electromagnetic absorbing materials. In *Advanced Materials for Electromagnetic Shielding: Fundamentals, Properties, and Applications*. Jaroszewski M, Thomas S, Rane AV, Ed. Hoboken, NJ, USA: John Wiley & Sons, Inc., 2018: 147–166.

[4] Yin PF, Zhang LM, Feng X, *et al*. Recent progress in ferrite microwave absorbing composites. *Integr Ferroelectr* 2020, **211**: 82–101.

[5] Neelakanta P. *Handbook of Electromagnetic Materials: Monolithic and Composite Versions and Their Applications*. Washington DC, USA: CRC Press, 1995.

[6] Green M, Chen XB. Recent progress of nanomaterials for microwave absorption. *J Materiomics* 2019, **5**: 503–541.

[7] Zeng XJ, Cheng XY, Yu RH, *et al*. Electromagnetic microwave absorption theory and recent achievements in microwave absorbers. *Carbon* 2020, **168**: 606–623.

[8] Liu JL, Zhang LM, Wu HJ. Electromagnetic wave-absorbing performance of carbons, carbides, oxides, ferrites and sulfides: Review and perspective. *J Phys D*: *Appl Phys* 2021, **54**: 203001.

[9] Zhang ZW, Cai ZH, Wang ZY, *et al*. A review on metal-organic framework-derived porous carbon-based novel microwave absorption materials. *Nano-Micro Lett* 2021, **13**: 56.

[10] Wang C, Han XJ, Xu P, *et al*. The electromagnetic property of chemically reduced graphene oxide and its application as microwave absorbing material. *Appl Phys Lett* 2011, **98**: 072906.

[11] Qi XS, Xu JL, Hu Q, *et al*. Metal-free carbon nanotubes: Synthesis, and enhanced intrinsic microwave absorption properties. *Sci Rep* 2016, **6**: 28310.

[12] Meng X, Lei WJ, Yang WW, *et al*. Fe_3O_4 nanoparticles coated with ultra-thin carbon layer for polarization-controlled microwave absorption performance. *J Colloid Interface Sci* 2021, **600**: 382–389.

[13] Yan L, Wang X, Zhao S, *et al*. Highly efficient microwave absorption of magnetic nanospindle-conductive polymer hybrids by molecular layer deposition. *ACS Appl Mater Interfaces* 2017, **9**: 11116–11125.

[14] Li X, Wen CY, Yang LT, *et al*. MXene/FeCo films with distinct and tunable electromagnetic wave absorption by morphology control and magnetic anisotropy. *Carbon* 2021, **175**: 509–518.

[15] Liang CY, Wang ZJ. Controllable fabricating dielectric-dielectric SiC@C core–shell nanowires for high-performance electromagnetic wave attenuation. *ACS Appl Mater Interfaces* 2017, **9**: 40690–40696.

[16] Zhao YJ, Zhang YN, Yang CR, *et al*. Ultralight and flexible SiC nanoparticle-decorated carbon nanofiber mats for broad-band microwave absorption. *Carbon* 2021, **171**: 474–483.

[17] Liu Y, Cui TT, Wu T, *et al*. Excellent microwave-absorbing properties of elliptical Fe_3O_4 nanorings made by a rapid microwave-assisted hydrothermal approach. *Nanotechnology* 2016, **27**: 165707.

[18] Luo J, Hu Y, Xiao L, *et al*. Synthesis of 3D flower-like Fe_3S_4 microspheres and quasi-sphere Fe_3S_4-RGO hybrid-architectures with enhanced electromagnetic wave absorption. *Nanotechnology* 2019, **31**: 085708.

[19] Zhang C, Wang B, Xiang J, *et al*. Microwave absorption properties of CoS_2 nanocrystals embedded into reduced graphene oxide. *ACS Appl Mater Interfaces* 2017, **9**: 28868–28875.

[20] Jia ZR, Lin KJ, Wu GL, *et al*. Recent progresses of high-temperature microwave-absorbing materials. *Nano* 2018, **13**: 1830005.

[21] Golla BR, Mukhopadhyay A, Basu B, *et al*. Review on ultra-high temperature boride ceramics. *Prog Mater Sci* 2020, **111**: 100651.

[22] Williams WS. Transition-metal carbides. *Prog Solid State Chem* 1971, **6**: 57–118.

[23] Williams WS. Transition metal carbides, nitrides, and borides for electronic applications. *JOM* 1997, **49**: 38–42.

[24] Williams WS. The thermal conductivity of metallic ceramics. *JOM* 1998, **50**: 62–66.

[25] Pierson HO. *Handbook of Refractory Carbides and Nitrides: Properties, Characteristics, Processing, and Applications*. New Jersey, USA: Noyes Publications, 1996.

[26] Zhou YC, Zhao B, Chen H, *et al*. Electromagnetic wave absorbing properties of TMCs (TM = Ti, Zr, Hf, Nb and Ta) and high entropy $(Ti_{0.2}Zr_{0.2}Hf_{0.2}Nb_{0.2}Ta_{0.2})C$. *J Mater Sci*

Technol 2021, **74**: 105–118.

[27] Chen H, Zhao B, Zhao ZF, *et al*. Achieving strong microwave absorption capability and wide absorption bandwidth through a combination of high entropy rare earth silicide carbides/rare earth oxides. *J Mater Sci Technol* 2020, **47**: 216–222.

[28] Zhang WM, Zhao B, Xiang HM, *et al*. One-step synthesis and electromagnetic absorption properties of high entropy rare earth hexaborides (HE REB_6) and high entropy rare earth hexaborides/borates (HE REB_6/HE $REBO_3$) composite powders. *J Adv Ceram* 2021, **10**: 62–77.

[29] Zhang WM, Zhao B, Ni N, *et al*. High entropy rare earth hexaborides/tetraborides (HE REB_6/HE REB_4) composite powders with enhanced electromagnetic wave absorption performance. *J Mater Sci Technol* 2021, **87**: 155–166.

[30] Zhang WM, Dai FZ, Xiang HM, *et al*. Enabling highly efficient and broadband electromagnetic wave absorption by tuning impedance match in high-entropy transition metal diborides (HE TMB_2). *J Adv Ceram* 2021, **10**: 1299–1316.

[31] Zhao ZF, Chen H, Xiang HM, *et al*. High entropy defective fluorite structured rare-earth niobates and tantalates for thermal barrier applications. *J Adv Ceram* 2020, **9**: 303–311.

[32] Sun YN, Xiang HM, Dai FZ, *et al*. Preparation and properties of CMAS resistant bixbyite structured high-entropy oxides RE_2O_3 (RE = Sm, Eu, Er, Lu, Y, and Yb): Promising environmental barrier coating materials for Al_2O_3f/Al_2O_3 composites. *J Adv Ceram* 2021, **10**: 596–613.

[33] Zhao ZF, Xiang HM, Chen H, *et al*. High-entropy $(Nd_{0.2}Sm_{0.2}Eu_{0.2}Y_{0.2}Yb_{0.2})_4Al_2O_9$ with good high temperature stability, low thermal conductivity, and anisotropic thermal expansivity. *J Adv Ceram* 2020, **9**: 595–605.

[34] Dong Y, Ren K, Lu YH, *et al*. High-entropy environmental barrier coating for the ceramic matrix composites. *J Eur Ceram Soc* 2019, **39**: 2574–2579.

[35] Wang YC, Zhang RZ, Zhang BH, *et al*. The role of multi-elements and interlayer on the oxidation behaviour of (Hf–Ta–Zr–Nb)C high entropy ceramics. *Corros Sci* 2020, **176**: 109019.

[36] Xiang HM, Xing Y, Dai FZ, *et al*. High-entropy ceramics: Present status, challenges, and a look forward. *J Adv Ceram* 2021, **10**: 385–441.

[37] Oyama ST. Introduction to the chemistry of transition metal carbides and nitrides. In *The Chemistry of Transition Metal Carbides and Nitrides*. Dordrecht, the Netherlands: Springer Netherlands, 1996: 1–27.

[38] Gubanov VA, Ivanovsky AL, Zhukov VP. *Electronic Structure of Refractory Carbides and Nitrides. Cambridge*, UK: Cambridge University Press, 1994.

[39] Cuppari M, Santos S. Physical properties of the NbC carbide. *Metals* 2016, **6**: 250.

[40] Castle E, Csanádi T, Grasso S, *et al*. Processing and properties of high-entropy ultra-high temperature carbides. *Sci Rep* 2018, **8**: 8609.

[41] Ye BL, Ning SS, Liu D, *et al*. One-step synthesis of coral-like high-entropy metal carbide powders. *J Am Ceram Soc* 2019, **102**: 6372–6378.

[42] Feng L, Fahrenholtz WG, Hilmas GE, *et al*. Synthesis of single-phase high-entropy carbide powders. *Scripta Mater* 2019, **162**: 90–93.

[43] Tilley RJD. *Understanding Solids*. Chichester, UK: John Wiley & Sons, Ltd., 2004.

[44] Quan B, Shi WH, Ong SJH, *et al*. Defect engineering in two common types of dielectric materials for electromagnetic absorption applications. *Adv Funct Mater* 2019, **29**: 1901236.

[45] Van Beek LKH. The Maxwell–Wagner–Sillars effect, describing apparent dielectric loss in inhomogeneous media. *Physica* 1960, **26**: 66–68.

[46] Mabbs FE, Collison D. *Electron Paramagnetic Resonance of d Transition Metal Compounds*. Amsterdam, the Netherlands: Elsevier Science Publishers B.V., 1992.

[47] Gonzales J, Gajare S, Nguyen S, *et al*. Magnetically tuning the loss tangent in $La(Al_{1-x}Fex)O_3$ using low field electron paramagnetic resonance transitions. *Appl Phys Lett* 2020, **117**: 222901.

[48] Jian X, Tian W, Li JY, *et al*. High-temperature oxidation-resistant $ZrN_{0.4}B_{0.6}$/SiC nanohybrid for enhanced microwave absorption. *ACS Appl Mater Interfaces* 2019, **11**: 15869–15880.

[49] Duan YP, Pang HF, Wen X, *et al*. Microwave absorption performance of $FeCoNiAlCr_{0.9}$ alloy powders by adjusting the amount of process control agent. *J Mater Sci Technol* 2021, **77**: 209–216.

[50] Duan YP, Wen X, Zhang B, *et al*. Optimizing the electromagnetic properties of the $FeCoNiAlCr_x$ high entropy alloy powders by composition adjustment and annealing treatment. *J Magn Magn Mater* 2020, **497**: 165947.

[51] Zhang WD, Zhang X, Zhu Q, *et al*. High-efficiency and wide-bandwidth microwave absorbers based on MoS_2-coated carbon fiber. *J Colloid Interface Sci* 2021, **586**: 457–468.